Seismoelectric numerical modeling on a grid

Seth S. Haines[1] and Steven R. Pride[2]

ABSTRACT

Our finite-difference algorithm provides a new method for simulating how seismic waves in arbitrarily heterogeneous porous media generate electric fields through an electrokinetic mechanism called seismoelectric coupling. As the first step in our simulations, we calculate relative pore-fluid/grain-matrix displacement by using existing poroelastic theory. We then calculate the electric current resulting from the grain/fluid displacement by using seismoelectric coupling theory. This electrofiltration current acts as a source term in Poisson's equation, which then allows us to calculate the electric potential distribution. We can safely neglect induction effects in our simulations because the model area is within the electrostatic near field for the depth of investigation (tens to hundreds of meters) and the frequency ranges (10 Hz to 1 kHz) of interest for shallow seismoelectric surveys.

We can independently calculate the electric-potential distribution for each time step in the poroelastic simulation without loss of accuracy because electro-osmotic feedback (fluid flow that is perturbed by generated electric fields) is at least 10^5 times smaller than flow that is driven by fluid-pressure gradients and matrix acceleration, and is therefore negligible. Our simulations demonstrate that, distinct from seismic reflections, the seismoelectric interface response from a thin layer (at least as thin as one-twentieth of the seismic wavelength) is considerably stronger than the response from a single interface. We find that the interface response amplitude decreases as the lateral extent of a layer decreases below the width of the first Fresnel zone. We conclude, on the basis of our modeling results and of field results published elsewhere, that downhole and/or crosswell survey geometries and time-lapse applications are particularly well suited to the seismoelectric method.

INTRODUCTION

Observations of seismoelectric phenomena have been reported by many authors in the last seventy years (Thompson, 1936; Martner and Sparks, 1959; Parkhomenko, 1971). A swell of experimental interest in the recent past (Thompson and Gist, 1993; Butler et al., 1996; Mikhailov et al., 1997; Garambois and Dietrich, 2001; Haines et al., 2003) suggests that the seismoelectric method could come into regular use soon, but reliable application to geophysical imaging remains elusive. The amassed literature indicates that seismoelectric phenomena definitely can be observed, and continued experimentation is encouraged.

Of most interest are the two seismoelectric modes described by Pride (1994) and Pride and Haartsen (1996) and discussed by Haines (2004): (1) the coseismic electric field within both compressional and Rayleigh waves that is created by accumulation and depletion of electrokinetic charge in regions of dilation and compression and (2) the electromagnetic interface response that occurs when a compressional wave or a shear wave encounters an interface in either the mechanical or electrical properties. It is worth noting that a shear wave, being equivoluminal, is not responsible for any charge accumulation in a homogeneous medium and so has no coseismic electric field associated with it; however, it does accelerate grains and create relative flow and, therefore, electrokinetic current. A shear wave thus has electrical current sheets in the plane of the wavefront that have small magnetic fields associated with them. Such fields generally are too small to measure, and we will not model them here. At an interface, a shear wave produces an imbalance of electrokinetic current across the interface that leads to charge accumulation on one side of the interface and depletion on the other; in other words, a shear wave, just like a compressional wave, induces electrokinetic dipoles at an interface.

Because the interface response is created at subsurface interfaces, it is the mode that generally is considered most useful for subsurface imaging. Field results (e.g., Butler et al., 1996; Haines, 2004) and theoretical predictions (Haartsen and Pride, 1997; Garambois and Dietrich, 2002) indicate that the interface response can provide useful information such as the locations of interfaces in flow properties and chemical contrasts, even from layers that are thinner than the seismic wavelength. Real progress beyond the current state of the science in seismoelectric prospecting, however, will likely require significantly more experimental complexity and an associated increase in expenses.

Many of the potential benefits and limitations of seismoelectric prospecting can be addressed through numerical simulation of the field experiments. Haartsen and Pride (1997) present a seismoelectric modeling algorithm for full three-dimensional (3D) wave propagation through one-dimensional (1D) (stratified) geologic models. They simulate the seismoelectric interface response from both lithological and fluid-chemistry contrasts (interfaces). Garambois and Dietrich (2002) use a similar algorithm to test seismoelectric sensitivity to contrasts in porosity, permeability, salinity, and pore-fluid viscosity. These results provide valuable insight into the types of contrasts that may be imaged with the seismoelectric method but do not provide any information about the effects of lateral subsurface heterogeneities on seismoelectric response. Because most realistic applications of the seismoelectric method (imaging of sand channels or time-lapse monitoring of oil reservoirs) involve complicated subsurface geometries, we need grid-based modeling algorithms to simulate realistic applications of the method. Such modeling capabilities will help provide synthetic data sets for designing and testing data-processing algorithms. Han and Wang (2001) provide an algorithm for finite-element modeling of the seismoelectric equations but limit their treatment to SH waves.

In this paper, we use numerical simulations to focus on how the seismoelectric method may best be used and on how target geometry variations alter the observed interface response. We present a finite-difference modeling algorithm that simulates seismoelectric phenomena in earth models with arbitrary heterogeneity but allows for all poroelastic wave modes (fast waves, slow waves, and shear waves). A two-dimensional (2D) implementation of this algorithm is given to test the effect of target geometry variations (layer thickness, lateral extent, and lateral position) on the observed seismoelectric response. We then present results from a downhole time-lapse survey simulation, which we consider to be an application that is particularly well suited to the seismoelectric method.

NUMERICAL ALGORITHM

Starting with the full set of equations governing the coupled seismic and electromagnetic response as derived by Pride (1994), we first define the physics taking place in the equations and then make a series of justified approximations to arrive at the final (reduced) set of equations that will be solved numerically. We then discuss the numerical solution procedure.

Full set of equations for all response fields

Assuming an $e^{-i\omega t}$ time dependence, the fully coupled seismoelectric governing equations are

$$-\omega^2 \rho \mathbf{u} = -\nabla P_c + \nabla \cdot \boldsymbol{\tau}^D + \omega^2 \rho_f \mathbf{w}, \tag{1}$$

$$\boldsymbol{\tau}^D = G\left(\nabla \mathbf{u} + \nabla \mathbf{u}^T - \frac{2}{3} \nabla \cdot \mathbf{u}\mathbf{I}\right), \tag{2}$$

$$-\begin{bmatrix} P_c \\ p_f \end{bmatrix} = K_U \begin{bmatrix} 1 & B \\ B & B/\alpha \end{bmatrix} \begin{bmatrix} \nabla \cdot \mathbf{u} \\ \nabla \cdot \mathbf{w} \end{bmatrix}, \tag{3}$$

$$\begin{bmatrix} -i\omega \mathbf{w} \\ \mathbf{J} \end{bmatrix} = \begin{bmatrix} k(\omega)/\eta_f & L(\omega) \\ L(\omega) & \sigma(\omega) \end{bmatrix} \begin{bmatrix} -\nabla p_f + \omega^2 \rho_f \mathbf{u} \\ \mathbf{E} \end{bmatrix}, \tag{4}$$

$$\nabla \times \mathbf{H} = -i\omega \varepsilon \mathbf{E} + \mathbf{J}, \tag{5}$$

and

$$\nabla \times \mathbf{E} = i\omega \mu \mathbf{H}. \tag{6}$$

These are Biot's (1962) equations for the solid displacements $\mathbf{u}$ and filtration displacements $\mathbf{w}$ (the relative fluid/grain displacement), along with Maxwell's equations for the electric and magnetic fields $\mathbf{E}$ and $\mathbf{H}$. The deviatoric stress tensor $\boldsymbol{\tau}^D$ is defined as $\boldsymbol{\tau}^D = \boldsymbol{\tau} + P_c \mathbf{I}$, where $\boldsymbol{\tau}$ is the total bulk stress tensor acting on the material, and P_c is the confining (or total bulk) pressure.

The three poroelastic constants (K_U, B, and α) are (1) the undrained bulk modulus K_U, defined as the ratio of the confining pressure change to the sample dilatation for a sealed sample; (2) Skempton's (1954) coefficient B, defined as the ratio of the fluid pressure p_f to the confining pressure increments under the same undrained conditions; and (3) the Biot and Willis (1957) constant α, defined as the ratio of confining pressure to fluid-pressure increments, under the condition that the sample volume does not change. A general exact relation between these three poroelastic moduli is $\alpha B = 1 - K/K_U$, where K is the drained bulk modulus (the bulk modulus under the condition that the fluid pressure does not change). Note that Biot's (1962) moduli C and M are exactly related to the above as $C = BK_U$ and $M = BK_U/\alpha$. Under the special restriction that the grains are isotropic and homogeneous within each sample of the porous material, Gassmann's (1951) fluid-substitution relations are available to us, which can be stated as

$$\alpha = 1 - \frac{K}{K_s}, \tag{7}$$

$$B = \frac{\alpha}{\alpha + \phi(K/K_f - K/K_s)}, \tag{8}$$

and

$$K_U = \frac{K}{1 - B\alpha}, \tag{9}$$

where K_f is the fluid's bulk modulus, and K_s is the bulk modulus of the solid grain material. The key parameter controlling all the electrokinetic coupling is L. All of the parameters and variables, along with their names and respective units of measurement, are shown in Table 1.

The electrokinetic coupling at work in seismoelectric response is the result of a nanometer-scale separation of charge in which a bound charge is fixed to the surfaces of the solid grains is balanced by a diffusively distributed free countercharge (ions) in the mobile layer of adjacent fluid. This charge separation is called the electric double layer.

Table 1. Variables and parameters used in equations.

Symbol	Meaning	Units
$\mathbf{A}$	Poisson finite-differencing operator	—
B	Skempton's coefficient	—
C_m	Salt concentration	mol/liter
$\mathbf{E}$	Electric field	V/m
F	Formation factor	—
G	Shear modulus	Pa
H	Claerbout's helix-derivative matrix	—
$\mathbf{H}$	Magnetic field	A/m
$\mathbf{I}$	Identity tensor	—
$\mathbf{J}$	Current density	A/m^2
k	Dynamic permeability	m^2
k_o	Steady-flow permeability	m^2
K	Drained bulk modulus	Pa
K_f	Fluid bulk modulus	Pa
K_s	Solid (grain) bulk modulus	Pa
K_U	Undrained bulk modulus	Pa
L	Electrokinetic coupling coefficient	A/(Pa m)
M_o	Source moment	J
n	Johnson parameter	—
p_f	Fluid pressure	Pa
P_c	Confining pressure	Pa
$\mathbf{q}$	Grain/fluid relative velocity	m/s
$s(t)$	Dimensionless source function	—
t	Time	s
$\mathbf{u}$	Grain displacement	m
v_p	P-wave velocity	m/s
$\mathbf{v}$	Grain velocity	m/s
$\mathbf{w}$	Grain/fluid relative displacement	m
α	Biot-Willis constant	—
δ	Dirac delta function	—
δ_{Biot}	Slow wave diffusive skin depth	m
δ_{EM}	Electromagnetic skin depth	m
ε	Electric permittivity	F/m
ε_f	Fluid electric permittivity	F/m
ε_o	Electric permittivity of vacuum	F/m
ζ	Zeta potential	V
η_f	Fluid viscosity	Pa s
λ	Wavelength	m
λ_U	Undrained Lamé modulus	Pa
μ	Magnetic permeability	H/m
μ_o	Permeability of vacuum	H/m
ρ	Bulk density	kg/m^3
ρ_f	Fluid density	kg/m^3
ρ_s	Grain density	kg/m^3
$\widetilde{\rho}_f$	Effective fluid inertia	kg/m^3
σ	Bulk electric conductivity	S/m
σ_f	Fluid electric conductivity	S/m
$\boldsymbol{\tau}$	Total bulk stress tensor	Pa
$\boldsymbol{\tau}^D$	Deviatoric stress tensor	Pa
$\boldsymbol{\tau}_s$	Isotropic stress tensor	—
ϕ	Porosity	—
Φ	Electric potential	V
ω	Angular frequency	rad/s
ω_t	Transition frequency	Hz

We now describe the two types of electrokinetic coupling that are present in the transport laws of equation 4. Seismic waves generate a force $-\nabla p_f + \omega^2 \rho_f \mathbf{u}$ that, in addition to driving a Darcy fluid filtration $(k/\eta_f)(-\nabla p_f + \omega^2 \rho_f \mathbf{u})$, also transports the diffuse charge of the double layer relative to the bound charge on the grain surfaces, resulting in a streaming electric current $L(-\nabla p_f + \omega^2 \rho_f \mathbf{u})$. Such generation of an electric current from an applied fluid-pressure gradient is known as electrofiltration and is responsible for so-called seismoelectric phenomena. Conversely, when an applied electric field $\mathbf{E}$ acts on a porous material, in addition to driving a conduction current given by $\sigma \mathbf{E}$, it also acts as a body force on the excess charge of the diffuse double layer, resulting in a net fluid filtration given by $L\mathbf{E}$. Such generation of a fluid filtration from an electric field is known as electro-osmosis, and it is responsible for so-called electroseismic phenomena. If the coupling coefficient L were set to zero, there would be complete decoupling between the poroelastic and electromagnetic response fields.

Pride (1994) obtains analytic expressions for the frequency dependence of the three porous-media transport coefficients: permeability $k(\omega)$, electrokinetic coupling coefficient $L(\omega)$, and electric conductivity $\sigma(\omega)$. The important relaxation in these coefficients is associated with the onset of viscous boundary layers in the pores; i.e., above a certain transition frequency ω_t, inertial forces in the pores begin to dominate the viscous shearing, except in a small boundary layer near the grain surfaces. The creation of such viscous boundary layers changes the amplitude and phase of the induced transport. The transition frequency is given by $\omega_t = \eta_f/(\rho_f F k_o)$, where η_f is the fluid viscosity, ρ_f is the fluid density, F is the electrical formation factor, and k_o is the steady-flow permeability (Pride, 1994). For typical rocks and soils, $\omega_t/(2\pi) > 10^5$ Hz, which lies far above the seismic bandwidth (~ 10 Hz to 1 kHz) of interest to us here.

Reduced set of equations for seismoelectric response

We now make a series of justified approximations that result in a reduced set of equations in which the poroelastic response can be determined independently from the electrical response. The wave-induced fluid-pressure gradients and particle accelerations then act as source terms in the electrical-response equations.

As noted above, the relaxations associated with the development of viscous boundary layers occur at frequencies far greater than the seismic band. As such, we are in the low-frequency limit that allows Pride's (1994) results for the transport coefficients to be written as

$$\frac{\eta_f}{k(\omega)} = \eta_f k_o - i\omega\rho_f F(1 + 2/n), \qquad (10)$$

$$L(\omega) = \varepsilon_f \zeta/(\eta_f F), \qquad (11)$$

and

$$\sigma(\omega) = \sigma_f/F. \qquad (12)$$

Here the zeta potential ζ describes the strength of the electric double layer at the grain/fluid boundary, and n is a dimensionless parameter that is close to eight in clean materials and is defined in the dynamic permeability of Johnson et al. (1987). We write $\widetilde{\rho}_f = \rho_f F(1 + 2/n)$ to denote the effective fluid inertia in Darcy's law in what follows. Although the inertial term $-i\omega\widetilde{\rho}_f$ has a negligible amplitude relative to η/k_o in the seismic band, it will not be set to zero in Darcy's law because it provides numerical stability in the explicit time-stepping fi-

nite-difference modeling to be used. Relaxation in the poroelastic moduli caused by to attenuation mechanisms (e.g., as modeled by Pride et al., 2004) are neglected here.

Not every term within the governing equations 1–6 must be included in seismoelectric numerical modeling. For example, the dielectric-displacement current $-i\omega\varepsilon\mathbf{E}$ can be neglected relative to the conduction current $\sigma\mathbf{E}$ because $\omega\varepsilon/\sigma < 10^{-4}$ throughout the seismic band and for materials of interest.

Most notably, for seismoelectric applications in which seismic waves are generating electric fields, one can neglect the electro-osmotic feedback by which the generated electric field acts on the electric double layers in the pores, retarding the seismically induced flow. The amplitude of this feedback effect is estimated by considering the electric field generated in a compressional wave propagating through a homogeneous material. In this case, the charge accumulating in the peaks and troughs of the wave generates an electric field that drives a conduction current that just balances the streaming current so that $\mathbf{J} = 0$. As such, equation 4 gives $\mathbf{E} = -(L/\sigma) \times (-\nabla p_f + \omega^2 \rho_f \mathbf{u})$, which allows Darcy's law, to be written as

$$-i\omega\mathbf{w} = \frac{k}{\eta_f}\left(1 - \frac{\eta_f L^2}{k\sigma}\right)(-\nabla p_f + \omega^2 \rho_f \mathbf{u}). \qquad (13)$$

The dimensionless correction term in the parentheses represents the electro-osmotic feedback and, for the materials of interest, typically will satisfy $\eta_f L^2/(k_o\sigma) < 10^{-5}$, which can be safely neglected relative to one. As such, the electro-osmotic feedback term $L\mathbf{E}$ is at most a tiny perturbation to the wave-induced fluid flow and can be neglected in Darcy's law. This fact allows the poroelastic response to be completely decoupled from the generated electric fields.

In preparation for rewriting the governing equations in the time domain, we use $\mathbf{q} = -i\omega\mathbf{w}$ to represent the Darcy filtration velocity, $\mathbf{v} = -i\omega\mathbf{u}$ to represent the solid's particle velocity, and $\boldsymbol{\tau} = \boldsymbol{\tau}^D - P_c \mathbf{I}$ to represent the total bulk stress tensor. When we invoke the above justified approximations, the seismoelectric equations are transformed to the time domain by using $-i\omega \to \partial/\partial t$ to obtain

$$\rho\frac{\partial \mathbf{v}}{\partial t} + \rho_f\frac{\partial \mathbf{q}}{\partial t} = \nabla \cdot \boldsymbol{\tau}, \qquad (14)$$

$$\rho_f\frac{\partial \mathbf{v}}{\partial t} + \tilde{\rho}_f\frac{\partial \mathbf{q}}{\partial t} + \frac{\eta_f}{k_o}\mathbf{q} = -\nabla p_f, \qquad (15)$$

$$\frac{\partial \boldsymbol{\tau}}{\partial t} = [\lambda_U \nabla \cdot \mathbf{v} + K_U B \nabla \cdot \mathbf{q}]\mathbf{I} + G[\nabla \mathbf{v} + (\nabla \mathbf{v})^T], \qquad (16)$$

$$-\frac{\partial p_f}{\partial t} = \frac{K_U B}{\alpha}[\alpha \nabla \cdot \mathbf{v} + \nabla \cdot \mathbf{q}], \qquad (17)$$

$$\nabla \times \mathbf{H} = \sigma\mathbf{E} + L\frac{\eta_f}{k_o}\mathbf{q}, \qquad (18)$$

and

$$\nabla \times \mathbf{E} = -\mu\frac{\partial \mathbf{H}}{\partial t}, \qquad (19)$$

where $\lambda_U = K_U - 2G/3$ is the undrained Lamé modulus of the porous material. Note that the poroelastic response (equations 14–17) now is completely decoupled from the electromagnetic response (equations 18 and 19). In Ampére's law (equation 18), the wave-induced Darcy flux $\mathbf{q}$ (normalized by the fluid mobility k_o/η_f) is the source for the converted electromagnetic fields.

Our applications in this study are to the shallow subsurface defined as depths of investigation d less than a few hundred meters. Because of this restriction, a further approximation is justified. By combining equations 18 and 19 and by assuming an $e^{-i\omega t}$ time dependence, the electromagnetic skin depth δ_{EM} that is associated with the inductive electromagnetic diffusion is seen to be $\delta_{EM} = 1/\sqrt{\omega\mu\sigma}$. Across the seismic band $[\omega/(2\pi) < 1 \text{ kHz}]$, and for the materials of interest to us, $\delta_{EM} > 1$ km.

It is standard to demonstrate, using the Green's tensor for Maxwell's equations (e.g., Hertz, 1893), that the near-field response defined by $d/\delta_{EM} \ll 1$ is exactly the quasi-static response. As such, our modeled electric fields in this study (satisfying $d/\delta_{EM} \ll 1$) are contained within the electrostatic near field of the electromagnetic disturbances, so that the effects of induction can be entirely neglected. This means that $\nabla \times \mathbf{E} = 0$ throughout the modeled region, and thus $\mathbf{E} = -\nabla \Phi$, where Φ is the electric potential. Taking the divergence of equation 18 gives the Poisson equation controlling Φ:

$$\nabla \cdot (\sigma \nabla \Phi) = \nabla \cdot \left(\frac{\eta_f L}{k_o}\mathbf{q}\right). \qquad (20)$$

We are not interested here in determining the magnetic fields because they are too small to be measured in field experiments ($|\mu_o\mathbf{H}|$ on the order of picoteslas). Note that although the source term on the right-hand side involves taking the divergence, any shear waves present nonetheless will act as electrical source terms at any interface where $\eta_f L/k_o$ changes. The electric field $\mathbf{E} = -\nabla \Phi$, determined from equation 20, is the total field generated from both compressional and shear waves.

To model the effect of an explosion at the source point $\mathbf{r}_s$, we add to the above stress tensor an additional isotropic stress tensor $\boldsymbol{\tau}_s$ that has the form

$$\boldsymbol{\tau}_s(\mathbf{r}, t) = s(t)M_o\mathbf{I}\delta(\mathbf{r} - \mathbf{r}_s), \qquad (21)$$

where $s(t)$ is a dimensionless source wavelet with a peak amplitude of one and M_o is the seismic moment release (units of energy). From our field experiments (e.g., Haines, 2004), we have determined that using $M_o = 400$ J for every kilogram of dynamite exploded produces synthetic (modeled) fields that are of comparable magnitude to the field measurements.

Numerical implementation

The poroelastic response that must be determined numerically is governed by equations 14–17, which represent the low-frequency limit of Biot's (1962) equations. Any stable algorithm that solves Biot's equations on a grid could be adopted. We choose to use a code developed by Chunling Wu at Stanford University (unpublished). Wu's code uses a 2D staggered grid and explicitly updates fields using second-order time differences, while determining spatial derivatives using the Fourier transform (a pseudospectral algorithm). The algorithm is similar to that of Ozdenvar and McMechan (1997). Following Cerjan et al. (1985), absorbing boundary conditions are achieved by smoothly ramping down the solid and fluid velocities, the bulk stress, and the fluid pressure in a 30-grid-point layer that surrounds all four sides of the modeling domain. Modeling the Dirac delta source function in 2D using the pseudospectral approach requires distributing the Dirac over four neighboring grid points (as opposed to just one grid point in the usual fourth-order spatial differ-

encing), placing a weight of $1/(4\Delta_x\Delta_z)$ on each of these grid points to represent the Dirac. No noticeable Gibbs phenomena are encountered in this method. Finite jumps in the material properties also can be present without noticeable Gibbs phenomena.

As shown by Pride and Garambois (2002), proper modeling of the fluid-pressure diffusion (Biot slow wave) around material-property contrasts is key to the proper modeling of the seismoelectric conversions. Modeling the Biot slow wave near an interface when Fourier transforms are used to calculate the spatial derivatives requires two or more grid points within the diffusive skin depth δ_{Biot} of the Biot slow wave. By inserting equation 15 into equation 17, one obtains the expression $\delta_{\mathrm{Biot}} \approx \sqrt{k_o K_U B/(\eta_f \alpha \omega)}$, where ω can be taken as the center circular frequency of the seismic pulse. In the simulations that follow, we work with a vertical grid spacing that always satisfies $\Delta_z < \delta_{\mathrm{Biot}}/4$. Most of the models were run with $\Delta_x = 7\Delta_z/5$. The usual Courant time-stability condition $\Delta_t < \Delta_z/(v_p\sqrt{2})$ is used to determine the time step Δ_t, where v_p is the fast P-wave velocity. In using this time discretization criterion, instability never was encountered. Chunling Wu's code has been tested, and it reproduces the exact known results for plane waves in homogeneous media.

The electromagnetic equations 18 and 19 also could be solved by explicit time differencing on a staggered grid to obtain both $\mathbf{E}$ and $\mathbf{H}$. However, as noted above, all electromagnetic fields in this paper are in the electrostatic near field of the interface generating a conversion. As such, we elect to solve the Poisson equation (equation 20) for the electric potentials Φ by using second-order finite-difference approximations in two dimensions. We do so following the approach of Claerbout (1998). After discretization, the operator $\nabla \cdot (\sigma\nabla)$ becomes a matrix we call $\mathbf{A}$, whereas the source term $\nabla \cdot (\eta_f L\mathbf{q}/k_o)$ becomes the 1D array called d, and we have the simultaneous set of equations $\mathbf{A}\Phi = d$ to solve for the electric potentials at all the grid points. However, this set of equations is rather poorly conditioned ($\mathbf{A}$ is far from being diagonal), and conjugate-gradient iterations converge slowly at best.

To improve the conditioning, we use the helix-derivative concept of Claerbout (1998). One defines a matrix H such that $H'H = R$, where R is the second-order differencing approximation of the negative Laplacian $-\nabla^2$ on the finite-differencing grid and where H' is the conjugate transpose of H. Claerbout (1998) finds an explicit expression for H that satisfies $H'H = R$. Using his helix-wrapping concept, in which the columns of a 2D matrix are unwound into a 1D array, he also is able to determine the inverse matrices (deconvolution operations) H^{-1} and H'^{-1}. One can identify the identity matrix as $I = H'^{-1}RH^{-1}$. Thus, to obtain a more diagonal system of equations, one rewrites $\mathbf{A}\Phi = d$ as

$$(H'^{-1}AH^{-1})H\Phi = H'^{-1}d. \qquad (22)$$

The matrix operation $H'^{-1}AH^{-1}$ is much better conditioned than the original matrix A. The simultaneous set of equations 22 then are solved for $H\Phi$ using conjugate gradients, and the potentials are obtained by filtering this result with H^{-1}. Stanford Exploration Project (SEP) free-software library (SEPlib, 2004) contains software for performing these operations. Finally, the electric fields are obtained by simple second-order finite differencing of $\mathbf{E} = -\nabla\Phi$. The electric fields are determined in the above manner after every tenth time step in the poroelastic code.

To allow for electric-potential boundary conditions, an additional 50 grid points are added to all sides of the primary model region to push the influence of those conditions away from the modeled region. Following Anderson and Woessner (1992), we increase the grid spacing by a factor of 1.3 from one grid point to the next, up to a maximum of 20 times the original grid spacing. The result is that the boundaries are at least as far from the modeled region as the modeled region is wide. On the distant boundaries, we invoke Neumann conditions $\partial\Phi/\partial n = 0$, where n is the direction normal to the boundary. To check the accuracy of the above algorithm for solving Poisson's equation, we have verified that the above procedure produces the exact known response of a dipole in a whole space.

2D MODELING RESULTS

In the following examples, we investigate the sensitivity of the seismoelectric interface response to the target geometry — layer thickness, lateral extent, and lateral position relative to the shot point. We also simulate a time-lapse downhole survey that takes advantage of several different properties of seismoelectric phenomena. As will be discussed, crosswell and vertical-seismic-profiling (VSP) (shot on the surface and electrodes downhole) layouts are particularly well suited to seismoelectric applications.

In the following simulations, the seismic source is modeled as a 1-kg shot of dynamite ($M_o = 400$ J). For the zeta potential (a key parameter that fixes the electrokinetic coupling coefficient L and, therefore, the amplitudes of the simulated electric fields), we use the model $\zeta = 0.01 + 0.025 \log_{10} C_m$ (volts), where C_m is the salt concentration in moles/liter of the fluid saturating the pores. This ζ model corresponds to laboratory measurements on sand (Pride and Morgan, 1991).

The pore fluid in all the examples is assumed to be water. For a sodium chloride electrolyte at room temperature, the electric conductivity of the fluid σ_f is $\sigma_f = 10\,C_m$ S/m, where C_m again is the salt concentration in moles/liter. The rock conductivity is given by $\sigma = \sigma_f/F$, where the formation factor is modeled using Archie's (1942) law $F = \phi^m$, and we assume $m = 2$ in all examples. The other fluid properties are $\varepsilon_f = 80\,\varepsilon_o = 6.8 \times 10^{-10}$ F/m, $\eta_f = 10^{-3}$ Pa s, $\rho_f = 10^3$ kg/m³, and $K_f = 2.2 \times 10^9$ Pa. The rock density is given by $\rho = \rho_f\phi + \rho_s(1 - \phi)$, with $\rho_s = 2.6 \times 10^3$ kg/m³. The incompressibility of the individual solid grains is taken to be $K_s = 35 \times 10^9$ Pa for sand and $K_s = 25 \times 10^9$ Pa for clay. None of the numbers given in this paragraph varies in the numerical examples. We use the Gassmann equations 7–9 to determine the poroelastic moduli. Thus, the only material properties that are allowed to vary in the following examples are K, G, ϕ, k_o, and C_m.

The poroelastic part of each simulation (for a 1024×1024 grid and 3500 time samples, such as is used for all the examples shown here) requires roughly 5 hours of computation on a single workstation. An electric-field simulation was carried out at every tenth one of these time steps (thus involving 350 calls to the Poisson-equation solver). This part of the seismoelectric modeling is readily parallelized (because each time step is independent of the others), but even running on 24 processors, the electric simulation of 350 time steps requires approximately 8 hours of computation.

Thickness and lateral extent of an aquitard

We begin with basic geometric variations of the simple model illustrated in Figure 1 that involves an interface at 30 m depth between a sand layer and a clay layer. Material properties for these layers are shown in Table 2. We are interested in the ability of the seismoelectric method to image thin subsurface layers, so we have run seismoelectric simulations with various thicknesses of the clay layer, ranging from a half-space (extending from 30 m deep to the base of the

model at 51 m) to 0.5 m thickness. These layers are represented by the dashed lines in Figure 1. The seismic source is modeled using a Ricker wavelet centered at 200 Hz. The discretization is Δ_z = 0.05 m, Δ_x = 0.07 m, and Δ_t = 13 μs.

A sample synthetic seismoelectrogram is shown in Figure 2a, for the case of a 2-m-thick clay aquitard. This shot gather has 96 channels of data, extracted from a depth of 0.5 m into the finite-difference model region (not in the absorbing layer). It represents the data that would be collected with an array of 1.4-m-wide electrode dipoles, with a spacing of 0.72 m between dipole centers, as shown in Figure 1. This synthetic gather shows the strongly dipping coseismic arrivals (labeled coseismic), as well as the flat interface response event from the aquitard (labeled IR). It also shows the coseismic arrival associated with the reflected P-wave (labeled Reflection CS). We also extract a seismoelectrogram from a depth of 50 m, representing a fan geometry as shown in Figure 2b. If the simulation cell is turned 90°, this example represents a gather that might be collected in a crosswell survey (seismic source in one well and electrodes in a line along the second well).

We can easily extract interface response arrival amplitudes from the fan (or crosswell) profile synthetic seismoelectrograms without interference from the strong coseismic arrivals. Figure 3 shows the absolute value of the amplitude of the maximum of the interface response arrivals for various layer thicknesses, each labeled. Note that for these synthetics, the amplitude of the coseismic fields ranges from ~4 to ~16 mV. We can observe the dependence of amplitude on layer thickness, and note that the observed amplitude is smallest

for the half-space. For the layer with thickness that is similar to the wavelength of the P-wave (~10 m, in this case), the two interface response events from the two sides of the layer are of opposite polarity, but the relative timing of the events causes them to constructively interfere. For layers that are thinner than the seismic wavelength, the two interface response events from the two sides of the layer no longer are separate events; instead, a single interface response event occurs that corresponds more to a single dipole situated on the layer. For the 5-, 2-, and 0.5-m-thick layers, we can see that the amplitude decreases with layer thickness, corresponding with the decreasing distance between the regions of electric-charge buildup. Even for the thinnest case (thickness=0.5 m or one-twentieth of the central wavelength), the interface response arrival is stronger than for the single-interface (half-space) model. This demonstrates the effectiveness of the seismoelectric method in detecting layers that are even 20 times smaller than the seismic wavelength. This result illustrates an essential difference between the seismoelectric interface response and a seismic reflection [which, for the $\lambda/20$ case, would have a much lower amplitude than the reflection from a single interface (Widess, 1973)].

Figure 2. Synthetic seismoelectrograms for the case of a 2-m-thick clay layer at 30 m depth. (a) Surface geometry shot gather, with coseismic energy recorded at the same time as the interface response (IR). The coseismic field of the reflected P-wave also is labeled. (b) Fan geometry gather, with the coseismic field arriving after the interface response.
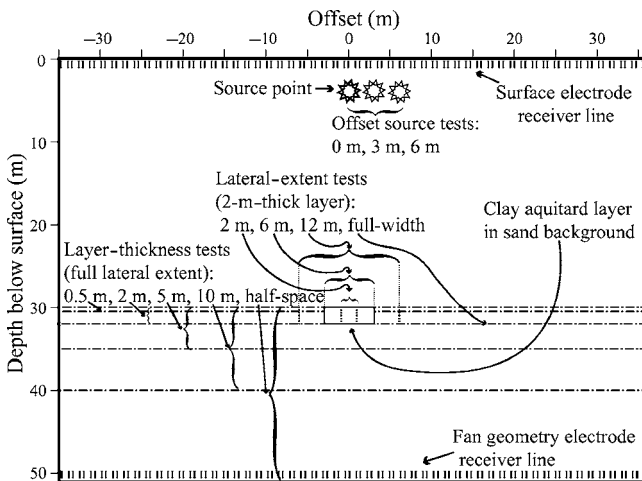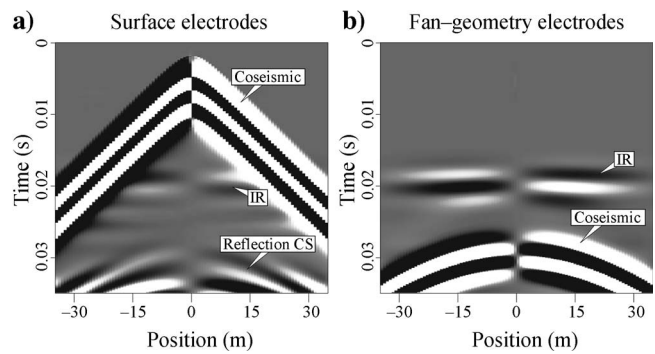

Figure 1. Schematic diagram showing the geometry used for synthetic models in this section. These models feature a clay aquitard layer at 30 m depth in a sand background. The layer thickness varies, as does its lateral extent. And for the case of a 2-m-thick, 6-m-wide layer, the shot position is varied. Data shown are for electrode receiver lines at the ground surface (surface geometry) and at depth in the model (fan geometry).
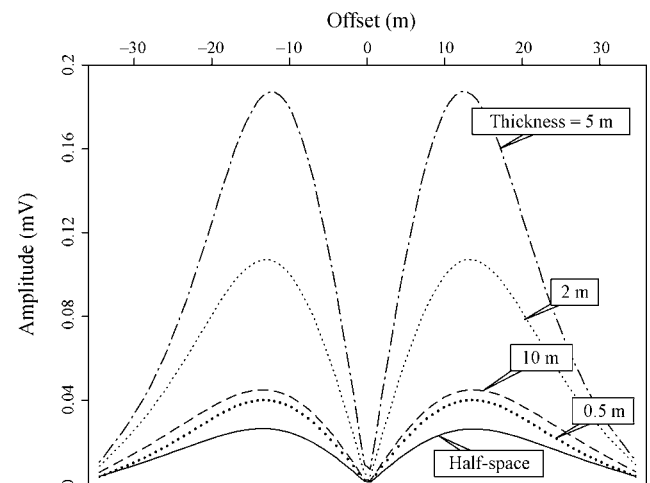

Figure 3. Graph of AVO for the peak of the interface response as measured by the fan receiver array for layers of various thicknesses, from a half-space to a half-meter. These amplitudes are roughly two orders of magnitude less than those of the modeled coseismic fields.

Table 2. Physical properties of materials in layer-thickness models.

	v_p (m/s)	ϕ (%)	K (GPa)	G (GPa)	k_o (m²)	σ (S/m)
Sand	1860	30	0.5	0.3	10^{-11}	0.01
Clay	2300	10	1.07	0.23	10^{-16}	0.05

We also are interested in the lateral resolution of the seismoelectric method, and so we have conducted a series of models with a 2-m-thick clay aquitard of variable lateral extent, ranging from a 2-m-wide block to a layer that is the full width of the model space. For all of these cases, the shotpoint is centered above the feature in question. Figure 4 shows amplitudes for the interface response from this series of targets. As the block becomes more laterally restricted, the resultant interface response decreases in magnitude. This result is not surprising, but it confirms that we can image narrow subsurface bodies, including those that are significantly narrower than the diameter of the first seismic Fresnel zone (which is ~24 m, in this case).

The amplitudes in Figure 4 are all for the case of a shotpoint that is centered above the layer of interest. Of course, this represents a fortuitous shot placement and is not the only geometry that will occur in a seismoelectric survey. For this reason, we investigate the effect of moving the survey laterally along the model space, as shown with the offset shot tests in Figure 1. Figure 5 shows amplitudes for the offset shots. Rather than decreasing for shots that are not directly above the target, the amplitude pattern is more complex. Because the target is not directly beneath the shot, the expanding seismic wavefront encounters the target at an angle that is oblique, rather than vertical, and the resulting interface response dipole is oriented at the same angle. The amplitude pattern that we observe (asymmetrical and not centered at the source point) corresponds with a dipole at the target that is pointing directly toward the seismic source. Unfortunately for the interpreter, this pattern is the same as for the interface response from a single dipping interface.

In both of these cases (shots located above a continuous dipping layer and near but not directly above the end of a discontinuous layer), the charge distribution that creates the interface response field is essentially a dipole oriented at the incidence angle of the seismic ray. The observed electric field will be very similar for these two cases, requiring multiple shotpoints to resolve the ambiguity.

Time-lapse sand-channel study

We now present an important application of the seismoelectric method to a problem of interest. Figure 6 shows the basic survey lay-

out. We are targeting a sand channel at 30 m depth within a clayey soil background. Material properties are shown in Table 3. The channel is 2 m thick and 6 m wide (the same geometry as one of the cases in the last section, but with the materials swapped). A well is located 5 m from the edge of the channel, and it allows us to use a vertical data-collection geometry, as shown in Figure 6. Data collected at one point in time (t0) are shown in Figure 7a, plotted in the usual way as for VSP data, with the depth axis vertical and the time axis horizontal. We can see the coseismic arrival, the coseismic field of the reflected P-wave (reflection CS), and the interface response created at the channel (IR). The coseismic field amplitude ranges from ~0.2 to ~2 mV, which is considerably lower than the coseismic fields in the previous section because of the much higher electrical conductivity of the material in which the field is being measured.

The downhole survey affords the opportunity to conduct a time-lapse survey with very similar recording conditions from one time to the next. What is changing with time in the model is the salt concen-

Figure 5. Graph of AVO for the peak of the interface response arrival from a 2-m-thick, 6-m-wide clay layer, with shot position varied from centered above the clay layer to offset 6 m from the center.
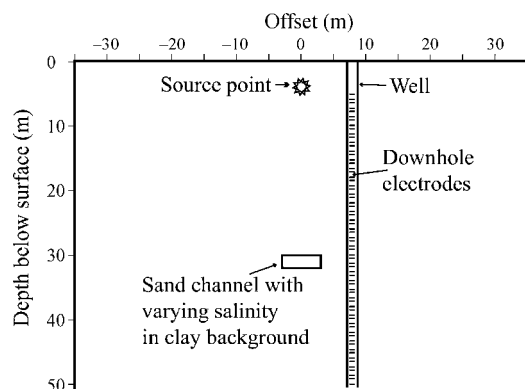
Figure 6. Schematic diagram of the model for the time-lapse synthetics. A sand channel (2 m thick and 6 m wide) lies at a depth of 30 m in a predominantly clay area. A well is 5 m from the edge of the layer, and we use a downhole electrode array to record shot gathers at three different points in time. The mechanical properties remain the same, but we simulate contamination by increasing the salinity of the pore water in the channel from 0.001 to 0.002 to 0.1 mol/liter.
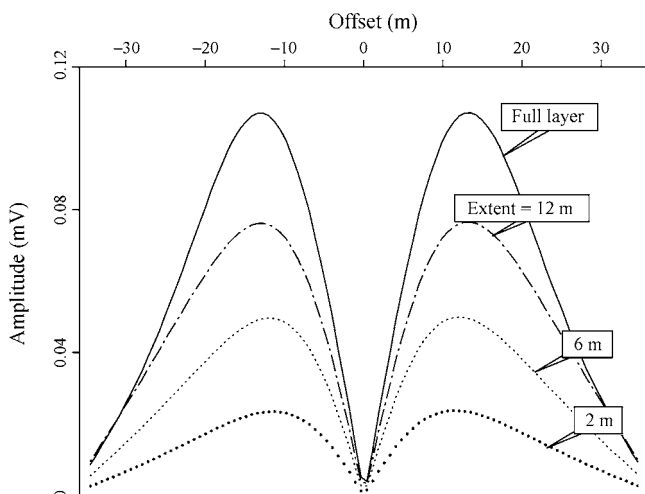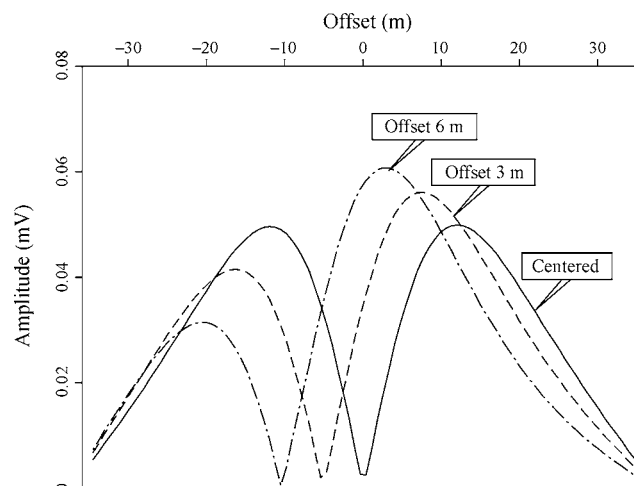

Figure 4. Graph of AVO for the peak of the interface response arrival from a 2-m-thick clay layer of varying lateral extent. These amplitudes are roughly two orders of magnitude lower than those of the modeled coseismic fields.

Table 3. Physical properties of materials in time-lapse models.

	v_p (m/s)	ϕ (%)	K (GPa)	G (GPa)	k_o (m²)	σ (S/m)	C_m (mol/L)
Sand, t0	1860	30	0.5	0.3	10^{-11}	0.01	0.001
Sand, t1	1860	30	0.5	0.3	10^{-11}	0.02	0.002
Sand, t2	1860	30	0.5	0.3	10^{-11}	1.0	0.1
Clay	2300	10	1.07	0.23	10^{-16}	0.05	0.001
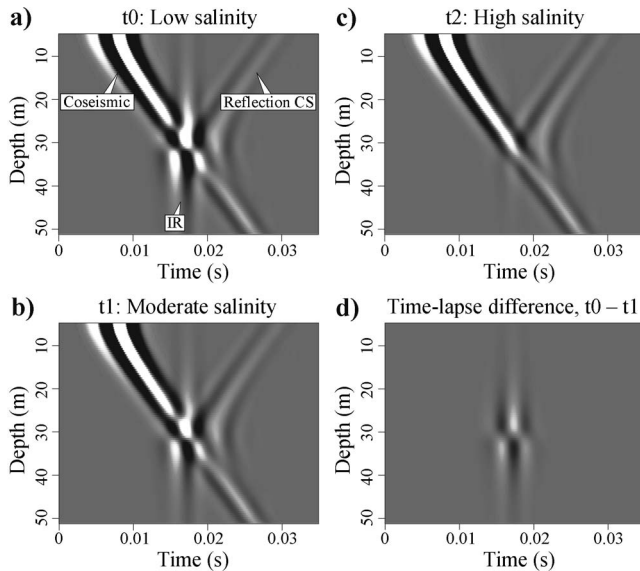
Figure 7. Synthetic seismoelectrograms for the time-lapse downhole study. (a) Starting case (time t0), with salinity of the pore water in the sand channel 0.001 mol/L. (b) At t1, the salinity has risen to 0.002, a small change that produces a noticeable change in the interface response. (c) At t2, the salinity is much higher (major contamination), and the interface response has nearly disappeared. (d) The time-lapse difference between t0 and t1, showing that the coseismic energy has been subtracted, leaving just the difference between the interface response arrivals.

tration of the water in the sand channel. This might correspond, for example, to a flux of pollutant through the channel. Because the water salinity has virtually no influence on the seismic waves, time-lapse surveying offers the possibility of simply differencing two shot gathers from different times to remove the coseismic energy.

Figure 7b shows data representing a later time (t1), when the pore fluid in the sand channel has become somewhat contaminated (the salinity has risen from 0.001 to 0.002 mol/liter). The interface response amplitude has fallen considerably, a change that is easily seen in the difference between the data collected at t0 (Figure 7a) and t1 (Figure 7b), plotted in Figure 7d. At a later point in time (t2), the contamination has worsened considerably, and the salinity of the channel porewater has become 0.1 mol/liter. The shot gather in Figure 7c shows that the interface response amplitude has decreased significantly. These changes also can be seen in the plots of the interface response amplitude differences between t0 and t1 and t2 in Figure 8. The magnitude of the amplitude change between t0 and t2 is similar to the magnitude of the coseismic fields, suggesting that it
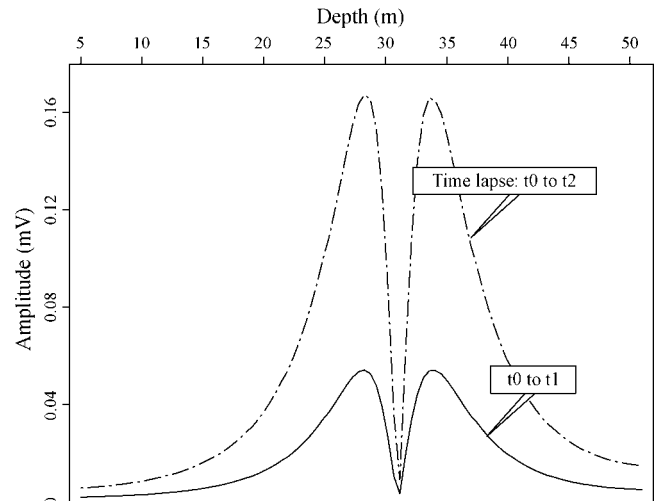

Figure 8. Graph of amplitude versus depth for the interface response arrival in the time-lapse survey simulation. Note that these amplitude changes are within one order of magnitude of the absolute amplitude of the coseismic fields, suggesting that they should be easily observable in real data.

likely would be readily observable in field data. The amplitude change between t0 and t1 is smaller but still is within an order of magnitude of the coseismic amplitude.

CONCLUSIONS

The numerical modeling presented in this paper is the first full seismoelectric simulation to be performed on a grid. The algorithm allows us to simulate targets and heterogeneity having arbitrary 2D heterogeneity. It thus allows us to simulate applications of the seismoelectric method with realistic subsurface heterogeneity. Such simulations will be valuable as we attempt to determine the best applications for the seismoelectric method. Our modeling results establish that the seismoelectric method can image layers that are thin (even for a layer of thickness $\lambda/20$, the interface response is stronger than for a single interface) and narrow (lateral extent much smaller than that of the first Fresnel zone). However, such images would likely consist of a single interface response arrival for the entire layer, rather than separate responses for the top and bottom of the layer, depending on the seismic wavelength.

The time-lapse simulation illustrates the potential for the seismoelectric method to provide useful information that is otherwise unavailable. The small sand-channel target at 30 m depth would be difficult to image seismically, and would be nearly impossible to image with ground-penetrating radar in this case because of the conductive clay, although at this depth any target would be a challenge for a surface radar survey. The change in salinity is essentially invisible seismically and would likely be difficult to characterize even with a resistivity survey that uses the borehole for single-well electrical resistivity tomography. This is the sort of application to which the seismoelectric method is uniquely well suited.

These results encourage continued field experimentation and provide guidance in experimental design. In particular, they highlight the value of creative survey geometries (e.g., the downhole geometry used in the last example). Coseismic fields often are more than an order of magnitude (and sometimes even are several orders of magnitude) stronger than the interface response fields of interest, so any

geometry that provides a clean time separation between the two in shot gathers is desirable. In addition to strengthening the observed signal by placing the receivers near the interface response dipole, the downhole geometry avoids noise from strong near-surface electric fields and, for a time-lapse study, downhole recording is likely to yield more uniform data recording because electrode coupling is likely to be more consistent than for electrodes in the soil. The target in the downhole example is particularly well suited to the time-lapse approach because the salinity change has virtually no effect on seismic wave propagation, so that the coseismic energy subtracts out of the gather differences.

This example also demonstrates a limitation of the seismoelectric method. If we had only the data from the single shot recorded by the downhole electrodes, it would be challenging to determine the lateral position and extent of the sand channel. Doing this would require modeling a dipole at each possible position of the sand channel (and oriented along the local seismic ray angle) and then fitting both the amplitude and the polarity reversals of the measured electric fields.

The utility of our numerical algorithm is limited by the high computational cost of each simulation. Three-dimensional data with sufficient shots to produce a seismoelectric image would be preferable to the 2D geometry shot gather simulations presented here. Improvements to the algorithm (particularly the preconditioning used for solving Poisson's equation) could offer substantial cost savings and would permit more complex simulations. In our synthetic examples, we have entirely neglected background electrical noise and instead have discussed amplitudes only relative to the coseismic energy.

Although it would be valuable to speak in quantitative terms, our results do not permit such interpretations. The amplitude of background noise can vary by an order of magnitude or more from site to site. Electrode coupling impacts the recorded S/N ratio but is difficult to simulate. Thus, our results serve to illustrate various qualitative concepts but cannot be taken as definite indications that the seismoelectric method is effective, for example, to a particular depth at every location. Such modeling is likely to be most useful in guiding the design of field experiments. Using the simulations as the forward model in attacking the inverse problem remains an exercise for the future.

REFERENCES

Anderson, M., and W. Woessner, 1992, Applied groundwater modeling: Academic Press Inc.

Archie, G. E., 1942, The electrical resistivity log as an aid in determining some reservoir characteristics: Transactions, American Institute of Mining, Metallurgical and Petroleum Engineers, **146**, 54–62.

Biot, M. A., 1962, Mechanics of deformation and acoustic propagation in porous media: Journal of Applied Physics, **33**, 1482–1498.

Biot, M. A., and D. G. Willis, 1957, The elastic coefficients of the theory of consolidation: Journal of Applied Mechanics, **24**, 594–601.

Butler, K. E., R. D. Russell, A. W. Kepic, and M. Maxwell, 1996, Measurement of the seismoelectric response from a shallow boundary: Geophysics, **61**, 1769–1778.

Cerjan, C. D., D. Kosloff, R. Kosloff, and M. Reshef, 1985, A nonreflecting boundary condition for discrete acoustic and elastic wave equations: Geophysics, **50**, 705–708.

Claerbout, J., 1998, Multidimensional recursive filters via a helix: Geophysics, **63**, 1532–1541.

Garambois, S., and M. Dietrich, 2001, Seismoelectric wave conversions in porous media: Field measurements and transfer function analysis: Geophysics, **66**, 1417–1430.

———, 2002, Full waveform numerical simulations of seismoelectromagnetic wave conversions in fluid-saturated stratified porous media: Journal of Geophysical Research, **107**, doi: 10.1029/2001JB000316.

Gassmann, F., 1951, Über die elastizität poröser Medien: Vierteljahrsschrift der Naturforschenden Gesellschaft in Zürich, **96**, 1–23.

Haartsen, M. W., and S. R. Pride, 1997, Electroseismic waves from point sources in layered media: Journal of Geophysical Research, **102**, 24745–24769.

Haines, S., 2004, Seismoelectric imaging of shallow tragets: Ph.D. thesis, Stanford University.

Haines, S., A. Guitton, B. Biondi, and S. Pride, 2003, Development experimental methods in electroseismics: 73rd Annual International Meeting, SEG, Expanded Abstracts, 560–563.

Han, Q., and Z. Wang, 2001, Time-domain simulation of SH-wave-induced electromagnetic field in heterogeneous porous media: A fast finite-element algorithm: Geophysics, **66**, 448–461.

Hertz, H., 1893, Electric waves: Macmillan Publ. Co..

Johnson, D. L., J. Koplik, and R. Dashen, 1987, Theory of dynamic permeability and tortuosity in fluid-saturated porous media: Journal of Fluid Mechanics, **176**, 379–402.

Martner, S. T., and N. R. Sparks, 1959, The electroseismic effect: Geophysics, **24**, 297–308.

Mikhailov, O. V., M. W. Haartsen, and M. N. Toksöz, 1997, Electroseismic investigation of the shallow subsurface: Field measurements and numerical modeling: Geophysics, **62**, 97–105.

Ozdenvar, T., and G. McMechan, 1997, Algorithms for staggered-grid computations for poroelastic, elastic, acoustic, and scalar wave equations: Geophysical Prospecting, **45**, 403–420.

Parkhomenko, E., 1971, Borehole and laboratory studies of the seismoelectric effect of the second kind in rocks: Izvestiya, Earth Physics, **9**, 663–666.

Pride, S., 1994, Governing equations for the coupled electromagnetics and acoustics of porous media: Physical Review B, **50**, 15678–15696.

Pride, S. R., J. G. Berryman, and J. M. Harris, 2004, Seismic attenuation due to wave-induced flow: Journal of Geophysical Research, **109**, B01201, doi: 10.1029/2003JB002639.

Pride, S. R., and S. Garambois, 2002, The role of Biot slow waves in electroseismic wave phenomena: Journal of the Acoustical Society of America, **111**, 697–706.

Pride, S. R., and M. W. Haartsen, 1996, Electroseismic wave properties: Journal of the Acoustical Society of America, **100**, 1301–1315.

Pride, S. R., and F. D. Morgan, 1991, Electrokinetic dissipation induced by seismic waves: Geophysics, **56**, 914–925.

SEPlib, 2004, Stanford Exploration Project, accessed August 1, 2006: http://sep.stanford.edu/software/SEPlib.

Skempton, A. W., 1954, The pore-pressure coefficients A and B: Geotechnique, **4**, 143–147.

Thompson, A. H., and G. A. Gist, 1993, Geophysical applications of electrokinetic conversion: The Leading Edge, **12**, 1169–1173.

Thompson, R. R., 1936, The seismic electric effect: Geophysics, **1**, 327–335.

Widess, M. B., 1973, How thin is a thin bed?: Geophysics, **38**, 1176–1180.